A & A m anuscript no. (will be inserted by hand later)	ASTRONOM Y
Y our thesaurus codes are: m issing; you have not inserted them	AND ASTROPHYSICS

An atlas of mid-infrared dust emission in spiral galaxies?

H.Roussel¹, L.Vigroux¹, A.Bosma², M.Sauvage¹, C.Bonoli³, P.Gallais¹, T.Hawarden⁴, J.Lequeux⁵, S.Madden¹, and P.Mazzei³

- 1 DAPNIA/Service d'Astrophysique, CEA/Saclay, 91191 Gif-sur-Yvette cedex, France
- ² Observatoire de Marseille, 2 Place Le Verrier, 13248 Marseille cedex 4, France
- 3 O sservatorio A stronom ico di Padova, 5 V icolo dell'O sservatorio, 35122 Padova, Italy
- Joint A stronom y C enter, 660 N.A 'ohoku P lace, Hilo, Hawaii 96720, USA
- ⁵ O bservatoire de Paris, 61 A venue de l'O bservatoire, 75014 Paris, France

Received 3 November 2000 / Accepted 23 January 2001

A b stract. We present maps of dust emission at 7 m and 15 m/7 m intensity ratios of selected regions in 43 spiral galaxies observed with ISOCAM. This atlas is a complement to studies based on these observations, dealing with star formation in centers of barred galaxies and in spiral disks. It is accompanied by a detailed description of data reduction and an inventory of generic morphological properties in groups de ned according to bar strength and H I gas content.

K ey words: atlas { galaxies: spiral { galaxies: ISM { infrared: ISM : continuum { infrared: ISM : lines and bands

1. Introduction

The mid-infrared maps presented here are part of a larger sample of nearby spiral galaxies analyzed in Roussel et al. (2001a and b: Papers I and II). Paper I primarily investigates the dynamical elects of bars on circum nuclear star form ation activity, studied through dust em ission at 7 and 15 m, and proposes an interpretation of these mid-infrared data in conjunction with information on molecular gas and stellar populations. Paper II deals with the use of mid-infrared uxes as a star form ation indicator in spiral disks. Observations belong to guaranteed tim e program s of ISO CAM, a cam era operating between 5 and 18 m onboard the satellite ISO (described by Cesarsky et al. 1996). The sample consists of a rst group of large and regular spirals, mainly barred, and of a second group of spiral galaxies belonging to the Virgo cluster. The angular resolution of 10^{00} (HPBW), combined with spectroscopic information from the same instrument, enables a detailed view of the variations of two dust phases (unidenti ed infrared band carriers and very sm all grains,

Send o print requests to:H.Roussel(e-mail:hroussel@cea.fr) $^{?}$ Based on observations with ISO, an ESA project with instruments funded by ESA Member States (especially the PI countries: France, Germany, the Netherlands and the United Kingdom) and with the participation of ISAS and NASA.

as characterized by e.g. Desert et al. 1990), tracing different physical conditions. A stellar contribution can also exist at 7 m (Boselli et al. 1998), but is negligible except in a few early-type galaxies.

The general description of the sample and detailed photom etric results are given in Paper I, where the spectra are also published. Here, we provide the details of observations and data reduction, total uxes at 7 and 15 m, a morphological description of galaxies grouped into appropriate categories and maps at 7 m, along with optical images. The 15 m maps have very similar morphology and are therefore not shown. These images demonstrate the peculiar character of circum nuclear regions seen in the mid-infrared. Information on the $F_{15}\!=\!F_7$ colors of bright complexes and other selected regions is added.

All of the maps are published for the rst time, except those of M 51 (Sauvage et al. 1996) and NGC 6946 (Malhotra et al. 1996), which are both re-analyzed here.

2.0 bservations

All galaxies were observed with two broadband Iters, LW 3 centered at 15 m (12{18 m) and LW 2 centered at 7 m $(5{8.5}$ m), that we shall hereafter designate by their central wavelength. Maps covering the whole infraredem itting disk were built in raster mode, with su cient overlap between ad acent pointings (half the detector eld of view in most cases) to avoid border artifacts and to provide redundancy for spoiled exposures. In all cases, the eld of view is large enough to obtain a reliable determ ination of the background level, except for NGC 4736 and 6744.NGC 5457, the largest spiral in the sample with an optical size of nearly 30°, was im aged with a combination oftwo overlapping observations made during dierent revolutions of the satellite. The pixel size is either 3^{00} or 6^{00} , depending on the galaxy size, but for Virgo galaxies it was always 6° , in order to increase the signal to noise ratio. The half-power/half-maximum diameters of the point spread function are respectively $6.8^{\circ\circ}/'$ $3.1^{\circ\circ}$ at 7 m with a $3^{\circ\circ}$ pixel size, $9.5^{\circ\circ}/5.7^{\circ\circ}$ at 7 m with a $6^{\circ\circ}$ pixel size, $9.6^{\circ 0}/3.5^{\circ 0}$ at 15 m with a $3^{\circ 0}$ pixel size and $14.2^{\circ 0}/6.1^{\circ 0}$ at 15 m with a $6^{\circ 0}$ pixel size. Table 1 sum marizes the relevant information regarding the observations.

To estim ate the relative importance of dierent emitting species in dierent galactic regions, spectral imaging between 5 and 16 m of the inner disks of vebright galaxies was also carried out. These observations are essential to interpret broadband imaging results. They consist of one pointing with two circular variable liters, from 16.5 to 9 m and from 9.6 to 5 m, with a spectral resolution = (FW HM) = 35 to 50. The sampling varies between 0.24 and 0.45 of (FW HM).

3.D ata analysis

3.1. Broadband Iter maps

Data reduction was performed using and adapting the ISOCAM Interactive Analysis package (CIA). The main diculty and source of uncertainty is the slow time response of the detector, which is typical of cold photoconductors. Below 20 K, the mobility of carriers becomes very slow, which generates long time constants, both in the bulk of the photoconductor and at contact electrodes. The typical time spent per pointing is $40\{100\,\mathrm{s\,w\,hereas}$ in general several hundred seconds are needed to reach stabilization within 10% of the ux step.

Several causes of m em ory e ects can be distinguished, although they always involve the same physics of the detector. We will use dierent designations for convenience: { (short-term) transients: they are due to the slow stabilization following a ux step (either upward or downward), after moving from one sky position to another; they are the origin of rem nant im ages seen after observing a bright source

{ long-term transients: drifts and oscillations visible during the whole observation and in uenced by previous history; contrary to short-term transients, no model exists to correct for them.

{ glitch tails: slow return to the sky ux level following the deposition of energy in the detector by intense cosm ic rays (this is an unpredictable e ect).

{ responsivity drops: they also follow cosm ic ray im pacts and produce \holes" which can last more than one hundred exposures (this is again an unpredictable e ect).

The data reduction proceeded in the following way:

- 1 { The subtraction of the dark current follows a model which predicts its time evolution for even and odd rows of the detector. It accounts for variations along each satellite orbit and along the instrument lifetime. 1
- 2 { If needed, we mask out the borders of the detector which are not su ciently illuminated to allow a proper at-elding.

3 { The removal of cosm ic ray impacts is complicated by the long-duration m em ory e ects they can produce. The arrival of an energetic cosm ic ray may be followed by either a slow ly decreasing tail or a responsivity drop, as explained above. The vast majority of glitches are, however, of short duration (one to three exposures) and can be rejected by median litering. To also remove small tails and plateaus induced by glitch pile-up, the exposures im m ediately surrounding exposures agged by the deglitcher were exam ined and their ux level compared with that of adjacent non-agged exposures, i.e. we iterated the median Itering once after rejecting the cosm ic ray peaks. This Itering cannot blindly be applied everywhere. First, at a step between a faint and a bright illum ination level and vice-versa, som e real signal variation m ay be m asked by the deglitcher. Therefore, the signal in the rst and last exposures for each sky position was compared with that in the neighboring exposures for the same sky position, and ags cancelled if necessary. Second, during a pointing on a bright peaked source such as galactic circum nuclear regions, the noise includes, in addition to the readout and photon noises, high am plitude uctuations which are approximately proportional to the signal and due to the satellite itter. For the purpose of glitch detection, an additional noise component proportional to the signal was thus tuned to reproduce the jitter e ects, and for very bright sources, de ned by a ux threshold set above the background, uctuations of 20% around the median ux were allowed. The memory e ects following some glitches, for which no model exists, are temporarily set aside and exam ined at step 6.

4 { Short-term transients are corrected for by using the latest available technique taking into account the detector characteristics (Coulais & Abergel 2000). The param eters of the model have been determined in low and uniform illum ination cases only, but are likely to vary with signal intensity and are inexact in the presence of strong spatial gradients. Indeed, when switching from a moderate ux level to a bright resolved source, the correction hardly modi es the data. A fler a large am plitude ux step, the stabilization is, however, faster, and thus the last exposures are likely closer to the real ux than in the case of small ux steps. The readout histories of pixels im aging galactic nuclei or extranuclear bright com plexes were carefully exam ined after step 7 to check whether the computed ux levelwas consistent with the level expected from the last valid exposures; if not, it was replaced with the mean signal in the last part of the readout history that was approxim ately at as a function of time. Furthermore, after seeing a bright source, rem nant im ages are not completely suppressed and can persist for several successive pointings; they are masked out at step 9.

5 { As long-term transients are not taken into account by the above correction, they were approximated and removed as one o set for each sky position, with respect to the last sky position taken as a reference, step by step

¹ It is described in \The ISOCAM dark current calibration report" by Biviano et al. (1998), which can be found at: http://www.iso.vilspa.esa.es/users/expl.lib/CAM_list.html.

backwards and assuming that all pixels follow the same evolution. This is done by comparing the median of the highest possible number of pixels seeing the o-source sky in the current pointing and in any of the already-corrected pointings, and selecting the same set of pixels in both, since at this stage the images have not been at-elded. As it is treated as an o set, the correction does not modify the source ux but attens the sky and allows better determination of the background level. It is similar to the long-term transient correction in the SLICE software of Mivile-Deschenes et al. (2000).

6 { Short-term transients after a strong downward ux step which were in perfectly corrected at step 4, or glitch tails, left aside at step 3, and with the strongest time derivatives (hence the easiest to detect), were masked out by an automatic procedure. Drops below the background level, due to a responsivity drop after a glitch, were also masked out (without the need for strong time derivatives to design an automatic rejection).

7 { The valid exposures were averaged for each sky position.

8 { The at-eld response was system atically determ ined for each pixel as its mean value when illuminated by the background emission (masking the source), and then normalized by the mean in the 12 12 central pixels. When for a given pixel the number of useable values is too low (which happens if the pixel mostly images the source, or is often rejected due to glitches or memory e ects), or when the error on the mean (computed from the dispersion) is higher than 5%, the at-eld response of this pixel is not computed as the mean, but interpolated using the neighboring pixels and the default calibration at-eld, before applying the normalization. This method produces better results than the use of raw calibration les. These calibration data were employed only for NGC 4736 and NGC 6744, for which the eld of view is too small to apply the above method (the background is hardly seen). For Virgo galaxies, which are small compared to the camera eld of view and were mapped with numerous pointings, a tim e-variable at-eld was estimated, improving the nal quality of the maps. The correction for long-term drifts (step 5) was then iterated once for all galaxies (this is again similar to the SLICE processing).

9 { The most conspicuous residualmemory e ects escaping rejection because they vary too slowly were removed manually in each sky position image. They were identified visually by comparing structure seen at the same sky coordinates in different overlapping pointings (corresponding to different sets of pixels with different histories), taking advantage of the spatial redundancy of the observations.

10 { The nalmap was built by projecting together all the individual images on a sky rectangular grid.

11 { The conversion from electronic units to spectral energy density units is made using the standard in ight calibration data base.

3.2. Spectral im aging

In order to be able to decom pose broadband observations according to the various em itting species, low-resolution spectra between 5 and 16 m were also obtained toward the inner 3^0 3^0 or 1.5^0 1.5^0 of ve galaxies. Table 2 sum m arizes the param eters of these observations.

For spectral im aging, the principles of data reduction are the same as for broadband. Iters. A dditional problem s encountered in this type of observation are the following: { The observation is split into two slightly overlapping parts: from 16.5 to 9.2 m and then from 9.5 to 5 m. The junction between the two circular variable. Iters, where the spectral transmission is low, can produce artefacts shortward of 9.2 m for a few wavelength steps, especially because of non-stabilization.

{ There is a small displacement of the source from one wavelength to another, the total shift reaching up to two 3^{0} -pixels, which is due to the rotation and change of the circular variable liters. This e ect was corrected for by thing the shape of the galactic central regions by a gaussian to measure their displacement on the array (for M 51, it was not possible and was done manually at the change between the two segments of the variable liter).

{ B right sources, such as galactic central regions, can create ghost im ages, due to re ections inside the instrument; in the case of NGC 1365, we could identify and isolate regions contam inated by obvious stray light ghosts. The ux collected by ghosts in a uniform illumination case is

20% (ISOCAM handbook)². For resolved sources, it depends on their position on the detector.

{ The at-eld response used ignores any time or wavelength dependency. Nevertheless, this source of error is negligible compared with memory elects and the error on the determination of the background level.

{ Probably due to an inaccurate dark current subtraction am pli ed by the transient correction algorithm, the shortwavelength spectrum can be negative at faint signal levels. { As sources occupy the whole eld of view and no spectra of empty regions were taken during the observations, the zodiacal foreground produced by interplanetary dust cannot be directly measured. We estimated it in the following way: we use a high signal to noise ratio calibration observation, from 16 to 5 m and then back from 5 to 16 m (which is useful to assess memory e ects), of an empty part of the sky. We apply an o set and a normalization to this zodiacal spectrum in order to obtain the maximum lower envelope to the average spectrum of the faintest pixels in our observation. The latter spectrum is composed of zodiacal light with superimposed faint emission bands (U IBs: see Paper I). Then, two bracketing zodiacal spec-

² ISO handbook volume III: CAM { the ISO camera, Siebenmorgen et al., 2000, SAI-99-057. It can be found at: http://www.iso.vilspa.esa.es/manuals/HANDBOOK/III/cam_hb/.

 $^{^3}$ The identi cation number of this observation, \TDT number" in the ISO archive, is: 06600401.

traw ith the same normalization are placed symmetrically; they are constrained to remain inside the dispersion limits of the observed spectrum, at least where it is not contaminated by U IBs. The minimum and maximum zodiacal spectra estimated in this way are subtracted from the galaxy spectrum, which produces an upper and a lower limit to the true spectrum. The minimum spectrum of the galaxy disk is also required to be positive, which tightens the bracketing of the zodiacal spectrum.

Due to the fact that the zodiacal light is several times higher than the disk spectrum (outside the bright central regions), the absolute intensity of the disk emission is subject to large uncertainties. However, since the zodiacal light spectrum is mainly featureless (it consists of a regularly rising part between 5 and 12 m and a slowly rising plateau from 11 to 16 m: see Fig. 1 in Paper I), the spectral shape of the disk em ission is well determ ined. { Because of ghosts, the at-eld response was not handled as in broadband liter observations. The observed signal is the sum of the source, the background and their respective ghosts, multiplied by the at-eld response: I = (S + b + g(S) + g(b)) ff. However, the calibration at-elds are also contam inated by ghosts: ffcal = (1 + g(b)=b). Therefore, we de ne the corrected signal as: $I_{corr} = (I \quad zodi \quad ff_{cal}) = ff_{lter}$, where zodi is the zodiacal spectrum estimated as described above and ff iter is a at-eld response measured with narrow 1ters, which does not contain any ghost. We then obtain $I_{corr} = S + g(S)$: only ghosts due to the source remain.

The spectra resulting from the data processing described above are shown in Paper I (for central regions, disks, and the zodiacal emission), where they are discussed. In Fig. 1 we reproduce the spectra of the galactic central regions, with their noise and uncertainty on the zodiacal foreground (but no estimation of the errors due to memory elects was possible). Contribution from straylight ghosts can be of the order of 10 {20% (see Sect. 3.5).

F ig.1. Spectra of the central regions of the ve galaxies observed in spectral imaging mode. They have been shifted for clarity by respectively 0.5, 1.3, 2.1 and 2.9 m Jy.arcsec 2 and multiplied by the numbers indicated on the right. Errors bars include the uncertainty on the zodiacal foregroung level, which is small with respect to the central source brightness.

3.3. Photom etry

In some observations, the background is high compared to the source surface brightness, and it can be a ected by inhom ogeneities largely due to an incomplete correction for both short-term and long-term memory e ects. The largest possible number of pixels has to be used, therefore, for a proper determ ination. In some other cases, a faint-levelem ission in spiralarms can be traced out to the m ap edge and likely continues outside the eld of view. However, this emission is extremely faint and does not introduce any signi cant error in integrated uxes. The only exceptions are NGC 4736 and NGC 6744, which are larger than the observation elds of view. For NGC 6744, 12% of the map in the southern part is blank, because the telescope did not move during 3 of the 16 program med pointings. The given total uxes are therefore lower lim its. O ther uncertain uxes are those of the apparent pair NGC 4567/68, which has slightly overlapping disks in projection.

For all galaxies, the integrated ux was measured in concentric circles and traced as a function of the number of pixels, after excluding some sectors of the map where the galaxy extends to large distances, so as to see as much uncontam inated background as possible. The background was tted in the linear part of this curve.

Total uxes are given in Table 1 and other photom etric results (see below) in Paper I.

3.4. Separation of central regions from disks

A common feature of dust emission distribution in our galaxies is a very strong central peak in a region of typically 1 to 3 kpc. Sub-structures are barely seen because the angular resolution is of the order of the size of these central regions, but can sometimes be suspected from variations in the infrared color $F_{15}=F_7$. We measured uxes from this central condensation after de ning its radius from the 7 m map. The galaxy center was rst determined by tting a two-dimensional gaussian on an appropriate zone whenever possible. O therwise, it was placed by visual criteria (for three galaxies). We computed the azim uthally averaged surface brightness pro le in elliptical annuli to compensate for the inclination on the sky, using as far as possible orientation parameters derived from detailed kinem atical analyses, otherwise from the position angle and axis ratio of outer isophotes. This pro lew as decom posed into a central region represented by a gaussian and an inner disk represented by an exponential. The scale param eters were tted on parts of the pro le devoid of any obvious structure, such as rings or spiral arm s, and each component was truncated at the radius where the exponential equals the gaussian, which de ned the photom etric aperture radius for the circum nuclear region, $R_{\,C\,N\,R}$.

Dilution e ects were corrected for in two ways. The rst consists of approximating central regions by point

sources and dividing the uxes measured inside R_{CNR} by the integral of the point spread function (PSF) inside the sam e aperture. The second one uses an iterative procedure. The image is rstre-sampled on a negrid (replacing each pixelby sm aller pixels all taking the sam e value). The brightest pixel of the original sam pling is looked for, the PSF centered on it is subtracted from both im ages with a smallgain to ensure convergence of the process (5% here), and is then replaced in the ne-grid in age with a gaussian containing the same ux as the rem oved PSF, of FW HM about half the pixel size. This procedure is analogous to the CLEAN algorithm used in radio astronomy (Hogbom 1974). This is repeated until the residual im age becomes reasonably uniform. For central regions not much more extended than the PSF, both estimates give equal results to a few percent; they dier in cases of a distribution atter than the PSF or in the presence of sub-structure, such as a ring.

Fluxes attributable to the pure spiral disk were then de ned as the di erence between total uxes and central region uxes measured in this way.

3.5. Errors and photom etric consistency

Photom etric errors cannot be computed rigorously, due to the uncontrolled memory e ects of the camera. The quoted uncertainties are therefore only indicative. They are the sum of three components:

- { the readout and photon noises added quadratically, computed from the readout history of each pixel;
- { the error on the background level tted to the histogram of o -source pixels (which includes uncertainties due to residuals of dark current, at-eld, glitches, rem nant im ages and long-term drifts), also added quadratically;
- { the deviation from stabilization, grossly estimated from the dynamics of each pixel's response during the time spent on each pointing, as half the dierence between the smoothed variation amplitude and the 99% condence level readout and photon noise. This error component is added linearly over all the pixels imaging the galaxy, because memory elects cannot be assimilated to white noise.

The latter error is usually dom inant, except for the faintest galaxies. We obtain typical errors of 10% at 7 m and 18% at 15 m (most galaxies having errors less than, respectively, 18 and 30%). These do not take into account ux density calibration uncertainties, which are of the order of 5%, with an additional 5% variation along each orbit (ISOCAM handbook).

The ve galaxies observed in spectral imaging mode provide the opportunity to perform checks on the agreement between uxes derived from independent observations. Since the wavelength coverage of our spectra (5 to about 16 m) does not contain the whole 15 m band (12)

Fig. 2.7 m uxes simulated from the spectra (ordinate) versus 7 m uxes measured in maps (abscissa). The apertures used are centered on the galactic nuclei and encompass the entire circum nuclear regions (chosen diameters of respectively 24° , 48° , 48° , 84° and 48° for NGC 613, 1097, 1365, 5194 and 5236). Note that the nucleus of NGC 5236 is slightly saturated in the 7 mmap. Error bars include deviation from stabilization for raster maps and the uncertainty on the zodiacal foreground level for spectra. The solid line indicates y = x and the dashed line y = 1.2x.

18 m), our comparison is limited to the 7 m band. We simulated observations in the LW 2 band (5{8.5 m) using its quantum e ciency curve. The comparison with the photometry performed on the 7 m maps is shown in Fig. 2. The agreement is perfect for NGC 1365, but the spectra of the other four galaxies system atically overestimate 7 m uxes with respect to raster maps. The amplitude of the deviation (23% for NGC 613, 16% for NGC 1097, 12% for NGC 5194 and 17% for NGC 5236) is of the order of what can be expected from stray light ghosts from the circum nuclear regions, which would be superim posed onto the source. This is consistent with the fact that an obvious ghost can be identied (outside the central regions) only in the case of NGC 1365, whose circum nuclear region is thus likely free from the ghost it generates. It should then be remembered that photom etry performed on raster maps is more reliable. See also Forster-Scheiber et al. (2001) for a photom etric com parison between ISOCAM and ISOSW S spectra.

Second, we can compare our results with independent measurements from the same ISOCAM raster observations (diering in the applied data reduction and photometry), for some galaxies of the sample analyzed by other individuals. In the Cambarre and Camspir samples, there is only one such galaxy, M 83, bright and very extended, for which Vogler et al. (2001) give $F_{15}=20\,2\,\mathrm{Jy}$ and $F_7=19\,3\,\mathrm{Jy}$, that is to say respectively 1.005 and 1.04 times the values obtained by us: the dierence is well within the error bars. The uxes of Virgo galaxies from Boselli et al. (1998) have not yet been published, so that we cannot check their consistency with ours.

We have also processed the 7 and 15 mm aps of several galaxies from the Sf.gk observation program (PIG. Helou), selected from the ISOCAM public archive and added to our sample for the analysis presented in Paper I. The maps are not presented here since they have been published in Dale et al. (2000) (DSH). The results of our

Fig.3. Comparison of our photom etric results at 15 m (top) and 7 m (bottom) with those of Dale et al. (2000) (DSH). Our error bars include the three components described above but not the systematic ux density calibration uncertainty, which acts equally on both sets of data. The solid line indicates y = x and the dotted lines y = (1 + x), with varying by steps of 0.1.

own photom etry are given in Paper I. Fig. 3 shows the confrontation of our uxes with those of DSH. NGC 6946, which is brighter by one order ofm agnitude than the other galaxies, is not included, for clarity (DSH obtain uxes within respectively 8% and 4% of ours at 15 and 7 m for this object). As seen in Fig. 3, whereas the agreement at 15 m is reasonable (for all galaxies except three, the dierence is less than 15%), the results at 7 m are dram atically discrepant, our uxes being system atically higher than those of DSH. As a result, $F_{15} = F_7$ colors computed by DSH are always higher than ours. To investigate the origin of this discrepancy, we perform ed some tests on NGC 986, an extended galaxy with bright circum nuclear regions, for which F_{15} (DSH) = $1.02F_{15}$ (us) and F_7 (DSH) = $0.64F_7$ (us).

We substituted each step of our data reduction successively, leaving all the other steps unchanged, according to what we thought DSH had done from the information they give on their data processing: use of calibration less for the dark current; use of the deglitcher described by Starck et al. (1999) with default parameters and without any subsequent masking; use of the \tau3" routine with default parameters for short-term transient correction; suppression of the long-term transient correction; and use of calibration less for the at-eld.

We would advise against the empirical \ t3" routine for photom etric purposes (it always nds a solution and articially produces corrected readout histories which are at, but this does not ensure that it converges toward the right value). Thus we initially thought that photom etric discrepancies would be attributable to the short-term transient correction. However, none of the changes listed

above is su cient to account for the large di erence in the 7 m $\,$ uxes.W e also tried to reproduce the photom etric m ethod of D SH , but this also can be excluded as the major source of the discrepancy.

As a last possibility, DSH mention that besides using calibration data, they also built at-elds using the observations them selves, by computing the median of the images { but apparently without previously masking the areas where the galaxy falls {; we do not know to which galaxies exactly this applies and in which instances they have instead used calibration les.We have thus explored this track and created such a at-eld for NGC 986.We not that this is the only way we can recover the 7 m ux given by DSH.

However, we emphasize that at-elds should not be built from the observations without masking the source, especially for an extended galaxy with bright central regions such as NGC 986, on a small raster: when doing so, one strongly overestimates the at-eld response at all the places where bright sources are observed (for the 2 raster of NGC 986 for instance, the nucleus is seen at four places on the detector, and still at three places if the rst sky position is removed, as DSH have done). As a consequence, after dividing by such a \ at-eld", the nal ux of the galaxy is severely underestim ated. If indeed DSH have proceeded this way, this could explain why their uxes are system atically lower than ours. If the sam e processing holds for 15 m maps, we speculate that the discrepancy with our 15 m uxes is reduced due to a compensation e ect by the background: at 15 m, the zodiacalem ission is much higher than at 7 m with respect to the galaxy ux (by a factor 5(6). Since the contrast between the background and the galaxy is much lower, the quality of the at-eld response is less a ected than at 7 m.

As a further check, one of us (M. Sauvage) independently reduced the maps and measured the uxes of NGC 986 by a method dierent to that explained in Sect. 3.3. At 7 m, allowing the isophotal detection limit to vary between 0 and 3 times the background dispersion above the background level, the resulting ux is within 6% and +8% of our tabulated ux, and the preferred measurement in view of the extension of the galaxy is at 4%. At 15 m, these numbers are respectively 14% and +13%, and 7%. Hence, our various estimates are in good agreement with each other.

4.M aps

For each galaxy are shown, from top to bottom: an optical map from the D igitized Sky Survey (with a better contrast inset from the second generation survey, if available and if the large-scale in age is saturated); the 7 m map, to which we applied a transfer function I^n , where 0.4 n 1, so as to make both faint and bright structures visible with the grey scale; $F_{15}=F_7$ colors of a few regions, selected for

being regular and bright at 7 or 15 m, which are shown as an illustration of the constancy of colors in disks, except in a few resolved star form ation complexes and in circumnuclear regions. For these colorm easurem ents, 7 m m aps were rst convolved to the 15 m angular resolution. As the astrom etry is not m ore precise than 10^{00} (the absolute accuracy of ISO, $1\{2^{00}$, is degraded by ISO CAM's lens wheel jitter), the displacement between both maps was m easured on central regions, by tting them with a gaussian when possible. For some V irgo galaxies not observed at 7 and 15 m in concatenated mode but during dierent revolutions, there is a rotation between the two maps of up to 5, which was estimated by thing the few usable regular com plexes with gaussians. A pertures were xed by the angular resolution: $w = chose 12^{00}$ for observations w ith a 3° pixelsize, and 18° for a 6° pixelsize, i.e. 1.25 times the half-power diam eter of the point spread function. We rst give the colors of the circum nuclear region inside the radius de ned as explained in Sect. 3.4 (m arked C'), and of the whole averaged disk (marked D'). Regions in the bar are noted B' and regions in arms, arcs or rings are noted A'. In some cases, the color of the central region inside the resolution unit is also given (Cr'). Fluxes are expressed in m Jy, so that to obtain a true ratio of powers em itted inside the 12{18 m and 5{8.5 m bandpasses (and not a ux density ratio), one should multiply $F_{15}=F_7$ by 0:42.

E mors on average disk colors include only photon and readout noises and the uncertainty on the background level; for all other color m easurem ents, they additionally contain an estimate of the errors due to incomplete stabilization. We again warm the reader that the latter error component cannot be derived rigorously: what follows is an attempt to provide an order-of-magnitude estimate. Since transients are of a systematic nature (the response of the camera to a given input is perfectly reproducible) and tend to behave coherently in a well de ned region (a brightness peak or minimum), we treated them in the following way:

{ We call m $_i$ the estim ated uncertainty due to memory e ects in the pixel i of the nalmap at the wavelength , derived as explained in the begining of Sect. 3.5.R is the ensemble of pixels belonging to the region of interest. Then the stabilization error on the true total ux F of that region is

$$M = M_{i2R}$$

{ We consider two cases: either both resulting errors at 7 and 15 m are treated positively, i.e. uxes are overestimated (we measure $F_{m \text{ es}}$ F + M instead of F), or both are treated negatively, i.e. uxes are underestimated ($F_{m \text{ es}}$ F M). We assume the same trend in both bands because memory elects are systematic in nature, and we consider it equally probable that uxes are overestimated or underestimated in the case of an upward ux

step as well as in the case of a downward step, because the detector response can oscillate as a function of time. { An asymmetric error bar on the color is then directly derived. Let us call M $_{+}^{c}$ and M $_{-}^{c}$ the bounds of this error bar: the measured color is noted $F_{mes}^{\ 15} = F_{mes}^{\ 7} = F_{mes}^{\ +M} = \frac{^{\circ}}{^{\circ}}$. If true uxes are overestim ated,

$$\begin{split} \frac{F_{\text{m es}}^{\ 15}}{F_{\text{m es}}^{\ 7}} &= & \frac{F^{\ 15}}{F^{\ 7}} & \frac{1+\ M^{\ 15}=\!\!F^{\ 15}}{1+\ M^{\ 7}=\!\!F^{\ 7}} \\ & \frac{F^{\ 15}}{F^{\ 7}} & 1+\ M^{\ 15}=\!\!F^{\ 15} & M^{\ 7}=\!\!F^{\ 7} \end{split}$$

using a lim ited developm ent. If D $_{\rm p}^{\rm c}$ is the deviation from the true color (F $_{\rm m}^{15}$ =F $_{\rm m}^{7}$ es $_{\rm m}^{\rm c}$ F $_{\rm m}^{15}$ =F $_{\rm m}^{\rm r}$) induced by an overestim ation of uxes and D $_{\rm m}^{\rm c}$ the deviation resulting from an underestim ation of uxes, one obtains

$$\mbox{D} \begin{tabular}{l} \mbox{C} \mbox{C} \mbox{E} = \begin{tabular}{l} \mbox{$F_{m \, es}$} \mbox{M} & \mbox{M}$$

and sim ilarly

$$D_{n}^{c} = \frac{F_{\text{mes}}^{15} + M^{15}}{F_{\text{mes}}^{7} + M^{7}} \qquad \frac{M^{15}}{F_{\text{mes}}^{15} + M^{15}} + \frac{M^{7}}{F_{\text{mes}}^{7} + M^{7}} :$$

{ There are four possibilities:

If $D_p^c > 0$ and $D_n^c < 0$ then $M_p^c = D_p^c$ and $M_p^c = D_n^c$. If $D_p^c < 0$ and $D_n^c > 0$ then $M_p^c = D_p^c$ and $M_p^c = D_n^c$. If $D_p^c > 0$ and $D_n^c > 0$ then $M_p^c = m$ ax $[D_p^c; D_n^c]$ and $[D_p^c = 0]$.

If $D_p^c < 0$ and $D_n^c < 0$ then $M_+^c = m$ in $[D_p^c; D_n^c]$ and $M_-^c = 0$.

M aps are organized as follows:

Fig. 5: strongly barred galaxies arranged in order of decreasing D $_{\rm bar}$ =D $_{\rm 25}$, the ratio of the deprojected bar diam eter to the disk diam eter;

Fig. 6: galaxies with weak or no bar arranged in the same order:

Fig. 7: the peculiar galaxies;

Fig. 8: all galaxies of the Virgo cluster sample whatever the bar strength which are not HI-de cient;

Fig. 9: H I-de cient V irgo galaxies.

M aps are oriented with north to the top and east to the left.

5.M orphological properties

In the following, we grouped galaxies according to their most striking property. The well-resolved regular spirals of the rst subsample were arranged in order of decreasing D $_{\rm bar}=$ D $_{25}$, the ratio of the deprojected bar diameter to the disk major diameter at the blue isophote 25 magarcsec 2 . Virgo galaxies are resolved with less detail, are more frequently highly inclined and intrinsically smaller and fainter, not allowing a meaningful measure of D $_{\rm bar}=$ D $_{25}$. They are separated into two groups dierentiated by interactions with the cluster environment: galaxies with a normal H $_{\rm I}$ content and H $_{\rm I}$ -de cient galaxies.

Beyond the complexity and distinctive features of all galaxies shown here, we choose to emphasize in this section the generic properties found within each group and do not describe in depth each individual object. The morphological types from the RC3 (de Vaucouleurs et al. 1991) are indicated.

We determined the size of the infrared emitting disk (at 7 $\,\mathrm{m}\,$ because the sensitivity is better than at 15 $\,\mathrm{m}\,$), de ned as the diam eter of the isophote 5 Jy.arcsec 2 . This is the deepest level that can be reasonably reached for all galaxies of the sample, corresponding to between one and ve times the background 1 uncertainty (except for NGC 5194 which has a higher background noise). This level is very similar to the sensitivity reached by Rice et al. (1988) in 12 m IRAS maps. The measure was performed on azim utally averaged surface brightness pro les, taking into account the orientation and inclination of the galaxy. We cannot see any dierence in the mid-infrared size to optical size ratio between barred and non-barred galaxies, but this ratio tends to increase from early-type to latetype galaxies. M ore fundam ental system atics exist as a function of gas content, which will be described in Sect. 6. Indeed, the likely reason for the observed dependence on Hubble type is the existence of a classication bias for HI-de cient galaxies: they are mostly classied as early type, due to the abnorm alaspect of their spiralarm s, and since the bulge-to-disk ratio criterion plays a minor role in the classication compared to the resolution of spiral arm s into star form ation complexes.

5.1. W ell resolved galaxies

{ Strongly barred spirals:

NGC 5383 (SBb), 7552 (SBab), 1433 (SBab), 1530 (SBb), 613 (SBbc), 1672 (SBb), 1097 (SBb) and 1365 (SBb).

The circum nuclear region is extremely bright in the mid-infrared { always brighter than any complex in the bar or the arm s. This is particularly obvious in NGC 7552, whose bar is relatively faint and where only a hint of the eastern arm is present, whereas emission from the large central region is very intense. All galaxies of this category are known to possess a nuclear spiral or ring, and sometimes additionally a nuclear bar. All except NGC 1433 have a hot-spot nucleus, i.e. giant star formation complexes within the central structure. We give here a brief sum mary of nuclear morphologies:

{ NGC 5383: nuclear spiral (Buta & Crocker 1993) with hot spots (Sersic 1973).

{ NGC 7552: nuclear ring (Feinstein et al. 1990) with hot spots { although the nucleus is classi ed am orphous by Sersic & Pastoriza (1965), bright complexes are clearly visible in the radio continuum maps of Forbes et al. (1994) {; Dottori & Pastoriza (1986) infer from a population synthesis of stellar absorption lines a cycle of three or four

successive starbursts.

{ NGC 1433: nuclear ring and nuclear bar (Buta 1986), am orphous nucleus (Sersic & Pastoriza 1965).

{ NGC 1530: nuclear spiral (Buta & Crocker 1993) with hot spots (Sersic 1973).

{ NGC 613: nuclear spiral and nuclear bar (Jungwiert et al. 1997), hot spots (Sersic 1973).

{ NGC 1672: nuclear ring with hot spots (Storchi-Bergmann et al. 1996), although Sersic & Pastoriza (1965) include it among amorphous nuclei.

{ NGC 1097: circum nuclear starburst ring of diam eter 20^{00} 1:5 kpc with hot spots, nuclear bar (Friedli et al. 1996). The ring is well resolved in the mid-infrared.

{ NGC 1365: nuclear spiral and nuclear bar (Jungwiert et al. 1997), hot spots (Morgan 1958).

The bar is detected in all galaxies but NGC 1433, which, besides its central region, displays only very faint and patchy em ission; in NGC 1365, it is detected but extrem ely di use.

W e also note that the mid-infrared emission of the bar generally consists of thin bands (as opposed to the stellar bar which is more oval), shifted towards the leading edge (if one assumes that spiral arms are trailing), in agreement with the response of other gas tracers to the bar potential. However, these bands do not coincide strictly with dust lanes seen in optical images: dust which is conspicuous in optical starlight absorption is not the same as dust seen in mid-infrared emission. In fact, absorbing dust lanes are signatures of gas density enhancements, at the location of shocks (Athanassoula 1992). As these shocks are strongest in the inner parts of the bar, near the central region, absorption dust lanes are also better developed and show higher contrast in the innerbar, independently of the brightness of the underlying stellar continuum (this is particularly well seen in NGC 1530 and 1672); conversely, the infrared em ission is system atically brightest in the outer parts of the bar and di use near the circum nuclear region. The same argument excludes signicant collisional excitation of dust in shocks: grains are heated by photons, including in regions of large-scale shocks.

A further sign of the di erent nature of absorption and em ission dust lanes is the aspect of the bar of NGC 1365: whereas absorption dust lanes show high contrast and are displaced far from the bar major axis toward the leading edge, the infrared em ission is extremely di use and rather symmetric about the major axis.

Star form ation complexes are generally seen in the bar at varying places, between mid-distance from the nucleus to the end of the bar (see for instance the bright knots in NGC 7552 and 1530). Such complexes inside the bar are also commonly found in Hobservations (Garca-Barreto et al. 1996; Martin & Friedli 1997). Emission is always enhanced at the junction between the bar and spiralarms, even in NGC 1433. This has been interpreted as an elect of orbit crowding, since it is the place where elongated orbits

subtended by the barm eet near-circular orbits of the disk (Kenney & Lord 1991). This region therefore favours star form ation, unlike the inner bar where the high-velocity shocks are likely to prevent it (Tubbs 1982; Athanassoula 1992; Reynaud & Downes 1998).

In som e galaxies (NGC 1530, 1365 and to a lesser extent NGC 5383), spiral arms are clearly seen to begin in advance of the bar, i.e. to continue beyond the junction with the bar towards the leading edge, which is never the case for weakly barred galaxies. This could be due to a decoupling between the bar and spiralwaves, i.e. dierent pattern speeds. Spiral arms generally make sharp angles with the bar (except the eastern arms of NGC 7552, 613 and 1672), which is also characteristic of strong bars, as already noted by P rendergast (1983).

The inner parts of arms show in most cases much star form ation, as evidenced by bright em ission and knots both in the optical and in the mid-infrared (exceptions are NGC 7552, whose western arm is not detected at all and whose eastern arm is hardly seen, and NGC 1433, whose entire inner ring is seen near the detection lim it. N evertheless, there seems to be a maximum radius encompassing sites of reasonable star form ation rates, outside of which spiral arms abruptly become fainter, both in optical and infrared im ages. The clearest and most symmetric example is NGC 1365, but this rem ark is valid for all. The exhaustion of outer arm s could be a signature of the corotation between the spiral wave and the gas, but it can also be related to the fact that all the strongly barred galaxies presented here are of early type (between SB ab and SBb, with one SBbc, NGC 613). This is not a bias in the sam ple: long bars are found predom inantly am ong early types (A thanassoula & Martinet 1980; Martin 1995).

We nally note the presence of an inner plateau or lens of di use infrared em ission delineating a sort of inner pseudo-ring in all galaxies of this group, again except NGC 7552 and 1433. In NGC 1530, the plateau is also seen in di use H em ission and the pseudo-ring materialized by H knots (Regan et al. 1996). In NGC 613, 1672 and 1097, a real lens is seen in the optical and further outlined by secondary tightly wound arms or incomplete arcs, best seen in the infrared.

{ W eakly or non barred spirals:

NGC 5236 (SABc), 6946 (SABcd), 4535 (SABc), 6744 (SABbc), 289 (SBbc), 5457 (SABcd), 4736 (SAab), 5194 (SAbc).

In weakly barred spirals, the central region is bright in the mid-infrared, but contrary to strong bar centers, it is relatively small and can be rivaled in brightness by complexes in the arm s. The centers of NGC 5236 and 6946 are particularly intense. Several of these galaxies also contain nuclear rings, but none seem s to harbor hot spots comparable to those seen in galaxies of the rst group. Here is a

list of nuclear m orphologies:

{ NGC 5236: nuclear ring (Buta & Crocker 1993), am orphous nucleus (Sersic & Pastoriza 1965).

{ NGC 6946: nuclear bar (Zaritsky & Lo 1986).

{ NGC 4535: nuclear ring (Buta & Crocker 1993).

{ NGC 6744, 289 and 5457: no rem arkable structure.

{ NGC 4736: weak nuclear bar (Mollenho et al. 1995).

{ NGC 5194: nuclear ring (Buta & Crocker 1993), which is seen in the mid-infrared.

The bar is detected in all SABs except NGC 6744, which is completely devoid of infrared em ission between the nucleus and the inner ring, much like NGC 1433.Unlike strong bars, weak bars do not contain infrared knots: their em ission is rather unstructured. They consist of thin lanes displaced towards the leading edge, just as in strong bars, but are more curved and smoothly connected to spiral arm s, in agreem ent with the notations of P rendergast (1983).

In NGC 6946, the bar is rather a fat oval distribution of stars, inside which a spiral arm can be traced at the north. The bar that we see in the infrared is shorter and rotated by as much as 35 to the leading side of the stellar oval. It does not coincide with the small northern arm but corresponds well to the 1^0 m olecular bar-like distribution (Ballet al. 1985; Regan & Vogel 1995), con med kinem atically by Bonnarelet al. (1988), and in which is embedded a nuclear bar rotated by a further angle of 15 to the leading side.

Zones at the junction between the bar and spiral arm s are much less conspicuous than in strongly barred galaxies (except the SE junction in NGC 289 which is bright). Brightness peaks are found further out along the arm s (see in particular NGC 4535). Dust emission follows remarkably closely the spiral structure at very large distances from the center. Note for instance the strong similarity between optical and infrared im ages of NGC 4535, where even the slight brightness enhancem ent at the northern edge of the disk, likely due to compression by the intracluster gas, is detected at 7 and 15 m. There is no sharp brightness decrease beyond some radius as in strongly barred spirals, except in NGC 289. This galaxy appears to be the closest of its category to strongly barred galaxies (bright knot at the end of the bar, rather sharp angle of spiral arm swith the bar, slight advance of the arm son the bar, abrupt decrease in surface brightness between an inner disk and an outer disk), despite its rather short bar. However, we note that the outer disk, whose size de nes the normalization to the bar size, is extremely tenuous, unlike in the other spirals of this group.

NGC 4736, although classi ed SA, has an oval distorsion revealed by its velocity eld (Bosma et al. 1977), hence a weak bar. Its m etallicity radial gradient is typical of SAB galaxies and could perhaps result from the past

m ixing e ects of a stronger bar now dissolved (M artin & B elley 1997).

{ Peculiar spirals:

NGC 1022 (SBa) and 4691 (SB 0/a).

NGC 4691 is described as an \irregular galaxy of the M 82 type" by Sandage (1961) and then as am orphous (Sandage & Bedke 1994), based on the chaotic, \intricate and extensive dust pattern in the central regions" which is similar to that in some starburst galaxies such as M 82 and suggests \galactic fountain activity". This interpretation is supported by the spectroscopic data of G are a-B arreto et al. (1995), whose I-band and H images also reveal a peculiar central structure with four knots. The two strongest H knots are resolved in our mid-infrared images, and are surrounded by two concentrations of molecular gas aligned with them, but at nearly twice the distance from the center (Wiklind et al. 1993). In the mid-infrared, we detect only the central structures and not the bar or the rest of the disk.

NGC 1022 is also peculiar and resembles NGC 4691 in many aspects. Both have extremely faint and smooth arm s and a chaotic system of dust laments, in all the interior of the inner ring for NGC 1022 (Sandage & Bedke 1994). NGC 1022 has a very short bar for a SBa galaxy. All interstellar tracers are highly concentrated in a small circum nuclear region (Garca-Barreto et al. 1991; Hameed & Devereux 1999) and we detect only this central region of size < 10^{00} 1 kpc in the mid-infrared. The morphology of both galaxies is suggestive of a past merger.

{ M agellanic barred spirals:

NGC337 (SBd) and 4027 (SBdm).

These are the two latest-type galaxies of the eld subsample. They are strongly asymmetric, with o -centered bars with respect to the outer isophotes. One arm harbors a very bright complex of star formation not far from its connection to the bar (this complex is clearly delineated in our mid-infrared images) and the second arm is embryonic. In some magellanic barred spirals, the bar center does not correspond to the kinematic center (but this is not the case for NGC 4027, according to Pence et al. 1988). This morphology is thought to be driven by tidal interaction (O dewahn 1994), or can result from the cooperation between spiral waves of modes m=1 and m=2 (Tagger & Athanassoula 1991), the two interpretations not being exclusive.

5.2. Virgo subsample

This subsample includes 9 or 10 spirals with normal H $_{\rm I}$ content and 14 or 13 H $_{\rm I}$ -decient spirals (NGC 4293 is at the lim it between the two categories). H $_{\rm I}$ -decient galaxies do not necessarily belong to the cluster core, but can be

found at large projected distances from M 87. For instance, NGC 4394, 4450, 4498 and 4580, with high H $_{\rm I}$ de ciencies, are located in the cluster periphery, between 1.3 and 2 M pc in projected distance from M 87.

Seven Virgo members of the sample have low blue or H-band luminosities (H data from Boselli et al. 1997, used because they give an indication on the total stellar mass), and their sizes are also intrisically small. They are either normal in their HI content (NGC 4351, 4430 and 4633) and of rather irregular morphology, except NGC 4634 seen edge-on, or decient with no obvious distorsion (NGC 4413, 4491, 4498 and 4506).

Interestingly, the galaxies presented in this paper which have a central $F_{15}=F_7$ ratio above 2 are all V irgo spirals (except NGC 1022), with large HI de ciencies. We computed the HI de ciency according to Guiderdoni & Rocca (1985) for the galaxies in our sample (the values are given in Paper I). This quantity is de ned as the logarithm ic di erence in HI m ass surface density between a reference eld galaxy sample and the galaxy considered, normalized by the dispersion in the eld sample. We have adopted as the threshold for HI dearth Def > 12 (Paper I). For all the galaxies with a central color $F_{15}=F_7>2$ exceptNGC 1022 (nam elyNG 4569,4293,4388 and 4491), 12 < D ef < 2. This suggests that the interaction with the intracluster gas also has consequences for the internal dynamics and reinforces the e ects of the bar. This is not a system atice ect, since the remaining 10 H I-de cient galaxies have low to moderate central colors.

6.0 ptical and m id-infrared disk sizes

W e have determ ined the size of the infrared em itting disk as explained at the beginning of Sect. 5, and also quantied the H $\scriptstyle\rm I$ de ciency, which is closely related to the anem is phenom enon (star form ation being inhibited in parts

Fig.4. Histogram s of mid-infrared to optical size ratios as a function of Hi-de ciency and morphological type. Def > 12 corresponds to severely Hi-stripped galaxies and Def < 0:3 to gas-rich galaxies.

of the outer disk where the gas density has dropped due to stripping). We not that the ratio of the infrared diam eter, D $_5^7$ J_V, to the optical diam eter D $_{25}$, de ned at the blue isophote 25 m ag arcsec 2 (de Vaucouleurs et al. 1991), shows marked variations as a function of H I de ciency (Fig. 4, top). Whereas D $_{5}^{7}$ Jy=D $_{25}$ is of the order of 0.7{0.9 for gas-rich spirals (none of the Virgo galaxies belongs to this category) and 0.96 for NGC 4634 which is seen edge-on, it ranges between 0.5 and 0.8 for spirals of interm ediate H I content, and between 0.35 and 0.65 for decient spirals, except 0.77 for NGC 4647 whose outskirts m ay be contam inated by the em ission of the neighbor elliptical NGC 4649. The value 0.35 is that of NGC 4569, known for its spectacular anem ia, and NGC 4438, which has undergone a violent collision (C om beset al. 1988). The only exception to this trend is NGC 289, which is very rich in H_I but has a ratio D $_{5}^{7}$ J_v=D $_{25}$ of about 0.4.W e again insist that its outer disk is of very low surface brightness, and that the condition for star form ation in such disks is likely to be very dierent from those in ordinary bright disk galaxies.

There is also a trend for D $_{5}^{7}$ $_{\rm Jy}$ =D $_{25}$ to be lower in early-type than in late-type spirals, as shown in Fig. 4 (bottom). However, this relationship is not independent of the rst one, since H I-de cient galaxies are mostly classi ed as early, due to the dominance in practice of the criterion based on the aspect of the arms in the Hubble-system classication (see Paper I). Early-type spirals are essentially characterized by smooth and faint outer disks, whereas in latest types, the arms are bright and patchy in their whole length, structured by star formation sites. Hence, a natural interpretation of both histograms shown here is that the ratio of mid-infrared to optical sizes primarily depends on the star formation activity in outer disks, which is strongly coupled to the gas density.

7.Sum m ary

We have presented complete maps of dust emission at 7 m of 43 galaxies spanning the spiral sequence from types $\rm SO/a$ to $\rm Sdm$, at an angular resolution less than $\rm 10^{00}$ and a sensitivity of the order of 5 Jy.arcsec 2 . We have also detailed the data reduction, provided the total uxes at 7 and 15 m and outlined the generic morphological properties in this sample. Since there exists an abundant literature on many of these galaxies studied individually, the present atlas has concentrated on common features. The detailed description of the sample and interpretation of the data are given together in Paper I.

The morphology is very similar in the mid-infrared and in the optical, except in peculiar galaxies where the dust emission is highly concentrated: the 7 and 15 memission follows tightly spiral arms, lenses and individual giant complexes. It appears however less extended than the stellar emission and tends to be reduced in smooth and unstructured spiral arms often seen in the outer disks of

early-type galaxies and especially of H I-de cient galaxies. This can be related to low densities of both the gas and the young stellar population. A nother noticeable di erence concerns the aspect of the bar, where the responses of the interstellar tracers and of the stellar component to the gravitational potential are clearly distinct. Finally, central regions stand out in our maps as entities with particular properties, and are studied in detail in Paper I.

The major characteristic of mid-infrared colors, i.e. 15 m to 7 m ux ratios, is that they are remarkably uniform throughout disks, except in some circum nuclear regions and a few bright complexes in spiralarms (the best example of the latter can be found in the outer interacting arms of M 101).

The maps will be made available to the community, in ts format, in the ISO public archive (http://www.iso.vilspa.esa.es/). They can be used for studies of the interplay between dust and other components of galaxies, and constitute the basis for two following papers.

Table 1.R aster observations. Listed are the number of the gure showing the maps, the project name (B:Cambarre; S:Cam spir; F:Sfgk; V:Virgo), the pixel size, the number of pointings projected onto the raster map, the eld of view, the number of exposures per pointing, the integration time per exposure, total on-target times at 15 and 7 m, and total uxes. When two gures are given, the rst one corresponds to 15 m and the second one to 7 m. For NGC 6946, observed with 6^{00} pixels, each pointing is displaced from the previous by a fractional number of pixels, so that the pixel size of the projected map is 3^{00} .

nam e	g.	proj.	pix.	N _p	m ap size	$n_{\text{exp}}^{}}$	t _{int}	T 15	Τ7	F ₁		F ₇	
			([∞])		([∞])		(s)	(5)		(m J	ſу)	
N 289	6c	В	3	16	240	26	5.0	2086.	2086.	327.8	25 . 6	342 . 9	14.7
N 337	7b	В	3	16	240	26	5.0	2131.	2137.	297.9	24.0	336.1	17.9
N 613	5c	В	3	25	288	25	5.0	3170.	3170.	1566.5	104.0	1473.3	71.4
N 1022	7a	В	3	16	240	26	5.0	2071.	2076.	802.3	86.4	444.4	45.3
N 1097	5d	В	3	25	288	25	5.0	3119.	3114.	2269.2	167.4	2128.6	125.
N 1365	5d	S	6	16	480	61	2.1	1978.	1984.	4436.7	764.5	3691.9	616.
N 1433	5b	В	3	25	288	25	5.0	3165.	3175.	355.3	41.0	381.3	33.8
N 1530	5b	В	3	16	240	26	5.0	2137.	2126.	606.1	39.2	573 . 9	39.1
N 1672	5c	В	3	25	288	25	5.0	3170.	3155.	2020.5	123.0	1985.0	129.
N 4027	7b	В	6	9	384	41,42	2.1	787.	787.	676.7	95.5	775.8	68.2
N 4027	75	ם	3	4	132	42,41	2.1	350.	359.	070.7	<i>33.</i> 2	775.0	002
N 4535	6b	В	6	16	480	27, 20	5.0	2066.	2056.	1127.9	181.4	1136.6	68.9
N 4333	0.0	Ь	3		132	26			534.	1127.9	101.4	1130.0	00.9
27.4601	-	_		4			5.0	539.		705.0	105.6	610 5	00.1
N 4691	7a	В	6	4	288	41, 42	2.1	359.	357.	795.9	185.6	613.5	83.1
37 4EOC 55 05	6:	_	3	4	132	42,41	2.1	352.	354.	4004 5	0.40	2012.5	005
N 4736 (M 94)	6d	S	6	9	288	20	5.0	917.	922.	4204.5	240.6	3913.9	225.
N 5194 (M 51)	6d	S	3	100	663	27	2.1	5384.	5390.	8003.2	493.5	8598.7	552.
N 5236 (M 83)	6a	S	6	49	768	21	5.0	4918.	5155.	20098.4	803.7	18474 . 9	899.
N 5383	5a	В	6	9	384	54	2.1	1024.	1022.	332 . 6	61.9	350.2	62.1
			3	4	156	54 , 52	2.1,5.0	459.	1083.				
N 5457 (M 101)												
main y	6c	S	6	49	j1302	20,21	5.0	4949.	4924.	5424.3	322.0	6034.0	116.
E arm y			6	25	j 972	25	5.0	3155.	3140.				
N 6744	6b	S	6	16	480	25	5.0	2031.	2041.	1497.4	125.7	2419.4	52.3
N 6946	6a	F	6–3	64	759	13,9	21,5.0	1585.	2872.	10651.6	1767.2	11648.8	678.
N 7552	5a	В	6	16	480	26	5.0	2091.	2112.				
			3	9	168	26	5.0	1184.	1174.	2767.6	193.7	1826.2	168.
V irgo cluster	sam ple	:											
4170	0		6	0.5	57.6	15 10	0.1	010	0.60	101 5	40.0	000 5	04.6
N 4178	8a	V	6	25	576	17, 18	2.1	819.	860.	181.5	48.0	228.5	24.6
N 4192	8a	V	6	49	768	17, 18	2.1	1528.	1625.	630.0	99.6	900.8	68.3
N 4293	9a	V	6	25	576	17 , 18	2.1	804.	844.	188.6	42.8	159.5	25.3
N 4351	8b	V	6	9	384	17 , 15	2.1	291.	283.	45.6	26.3	52 . 6	8.7
N 4388	9a	V	6	25	576	17 , 18	2.1	812.	863.	1008.2	244.0	499.4	77.8
N 4394	9b	V	6	16	480	16	2.1	480.	478.	139.0	41.0	161.2	19.1
N 4413	9b	V	6	9	384	17 , 16	2.1	302.	281.	93.0	31.4	89.3	11.0
N 4430	8b	V	6	9	384	17 , 16	2.1	294.	279.	98.0	23.5	132.5	13.9
N 4438	9c	V	6	49	768	17, 18	2.1	1528.	1629.	209.1	34.7	231.9	26.9
	9c	V	6	25	576	17	2.1	791.	844.	169.7	42.5	185.1	
N 4450		V	6	9	384	17, 15	2.1	310.	287.	81.1	25.2		7.6
N 4450 N 4491	9d			16	480	16	2,1	493.	478.	94.6	19.2		11.8
N 4491	9d 9d	V	Ю					294.	277.	12.7	5.2	21.1	9.8
N 4491 N 4498	9d	V V	6 6			17, 16	Z, . I			·	~ —		
N 4491 N 4498 N 4506	9d 9e	V	6	9	384	17 , 16	2.1 2.1			293 4		317 9	164
N 4491 N 4498 N 4506 N 4567/	9d					17, 16 17, 18	2.1	779.	829.	293.4 1099.0	15.5	317 . 9	
N 4491 N 4498 N 4506 N 4567/ N 4568	9d 9e 8c	V V	6 6	9 25	384 576	17, 18	2.1	779.	829.	1099.0	15.5 127.6	1074.7	
N 4491 N 4498 N 4506 N 4567/ N 4568 N 4569	9d 9e 8c 9e	V V	6 6	9 25 64	384 576 864	17 , 18	2.1	779. 1864.	829. 2108.	1099 . 0 939.3	15.5 127.6 125.1	1074.7 843.5	64.8 54.1
N 4491 N 4498 N 4506 N 4567/ N 4568 N 4569 N 4579	9d 9e 8c 9e 9f	V V V	6 6 6	9 25 64 36	384 576 864 672	17, 18 16, 18 17, 19	2.1 2.1 2.1	779. 1864. 1161.	829. 2108. 1306.	1099.0 939.3 619.2	15.5 127.6 125.1 85.1	1074.7 843.5 672.5	64.8 54.1 37.5
N 4491 N 4498 N 4506 N 4567/ N 4568 N 4569 N 4579 N 4580	9d 9e 8c 9e 9f	V V V V	6 6 6 6	9 25 64 36 9	384 576 864 672 384	17, 18 16, 18 17, 19 17, 16	2.1 2.1 2.1 2.1	779. 1864. 1161. 298.	829. 2108. 1306. 279.	1099.0 939.3 619.2 103.9	15.5 127.6 125.1 85.1 24.2	1074.7 843.5 672.5 102.6	64.8 54.1 37.5 7.7
N 4491 N 4498 N 4506 N 4567/ N 4568 N 4569 N 4579 N 4580 N 4633/	9d 9e 8c 9e 9f 9f 8c/	V V V	6 6 6	9 25 64 36	384 576 864 672	17, 18 16, 18 17, 19	2.1 2.1 2.1	779. 1864. 1161.	829. 2108. 1306.	1099.0 939.3 619.2 103.9 30.0	15.5 127.6 125.1 85.1 24.2 9.5	1074.7 843.5 672.5 102.6 30.3	64.8 54.1 37.5 7.7 9.1
N 4491 N 4498 N 4506 N 4567/ N 4568 N 4569 N 4579 N 4580	9d 9e 8c 9e 9f 9f 8c/	V V V V	6 6 6 6	9 25 64 36 9	384 576 864 672 384	17, 18 16, 18 17, 19 17, 16	2.1 2.1 2.1 2.1	779. 1864. 1161. 298.	829. 2108. 1306. 279.	1099.0 939.3 619.2 103.9 30.0 258.2	15.5 127.6 125.1 85.1 24.2	1074.7 843.5 672.5 102.6	64.8 54.1 37.5 7.7
N 4491 N 4498 N 4506 N 4567/ N 4568 N 4569 N 4579 N 4580 N 4633/	9d 9e 8c 9e 9f 9f 8c/	V V V V	6 6 6 6	9 25 64 36 9	384 576 864 672 384	17, 18 16, 18 17, 19 17, 16	2.1 2.1 2.1 2.1	779. 1864. 1161. 298.	829. 2108. 1306. 279.	1099.0 939.3 619.2 103.9 30.0	15.5 127.6 125.1 85.1 24.2 9.5	1074.7 843.5 672.5 102.6 30.3 278.3	64.8 54.1 37.5 7.7 9.1
N 4491 N 4498 N 4506 N 4567/ N 4568 N 4569 N 4579 N 4580 N 4633/ N 4634	9d 9e 8c 9e 9f 9f 8c/	V V V V V	6 6 6 6	9 25 64 36 9 36	384 576 864 672 384 672	17, 18 16, 18 17, 19 17, 16 17, 19	21 21 21 21 21	779. 1864. 1161. 298. 1123.	829. 2108. 1306. 279. 1266.	1099.0 939.3 619.2 103.9 30.0 258.2	15.5 127.6 125.1 85.1 24.2 9.5 40.7	1074.7 843.5 672.5 102.6 30.3 278.3	64.8 54.1 37.5 7.7 9.1 35.0 17.2

Table 2.Param eters of the spectral observations. They include the pixel size, the ratio of the eld of view to that of raster maps, the number of exposures per wavelength, the integration time per exposure and the total useful time.

nam e	pix.size ([®])	frac, size	n _{exp}	t _{int} (s)	T _{tot} (s)
N 613ª	3	0.33	12	2.1	3960.
N 1097 ^b	6	0.66	9{10	2.1	3276.
N 1365	6	0.40	15	2.1	4918.
N 5194	6	0.29	15	2.1	4918.
N 5236	6	0.25	15	2.1	4918.

^a At 3° , no calibration at-eld in narrow lters was available, so we did not apply the division by ff lter (see last paragraph of Section 32).

 $^{^{\}rm b}$ At the change of variable liter at 9.2 m, a downward jump was visible in the whole eld; to cancel it, we applied a unique o set to the second part of the spectrum .

Fig. 5: Strongly barned galaxies by order of decreasing bar strength. a: NGC 5383 and 7552, with D $_{\rm bar}=D_{25}$ 0:65 and 0.67. In all gures are displayed, from top to bottom: an optical im age from the DSS with, in a corner, a segment showing the orientation of the line of nodes and the inclination value; the 7 m map; $F_{15}=F_7$ colors of selected regions (C': circum nuclear region; D': averaged disk; 'Cr': central resolution element). Locations in the bar (B') or the arm s (A') are indicated on the 7 m map, which is scaled identically to the optical map except when a dashed segment outlines the eld of view shown below.

Fig. 5:b:NGC 1433 and 1530, with D $_{\rm bar}\!=\!$ D $_{25}$ $\,$ 0:54 and 0.48.

Fig. 5:c: NGC 613 and 1672, with D $_{\rm bar}$ =D $_{25}$ 0:45 and 0.42.

Fig. 5:d:NGC 1097 and 1365, with D $_{\rm bar}$ =D $_{25}$ 0:35 and 0.31. The labels S' and N' correspond to the brightest spot in the ring and the nucleus, whose colors were estimated from the images treated with the analog of CLEAN (Sect. 3.4), with no error bars.

Fig. 6:W eakly barred and unbarred galaxies.a:NGC 5236 and 6946, m oderately barred with D $_{\rm bar}\!\!=\!\!D_{25}$ 0.24 and 0.19.

Fig. 6: b: NGC 4535 and 6744, weakly barred with D $_{\rm bar}\!=\!\!D_{25}$ 0:18 and 0.17.

Fig. 6: c: NGC 289 and 5457, w ith D $_{\rm bar}$ =D $_{\rm 25}$ 0:15 and 0.06.

Fig. 6: d: NGC 4736 and 5194, unbarred galaxies (NGC 4736 possesses in fact an oval distorsion). The labels N' and Cp' refer to the nucleus of NGC 5194 and the nucleus of its companion, NGC 5195. Note that in NGC 5194, the thin NE and SW outermost parts of both arms seen in the mid-infrared coincide with dust lanes seen in absorption.

Fig. 7: Peculiar galaxies. a: NGC 1022 and 4691, am orphous barred spirals (possibly m erger results). They have D $_{\rm bar}$ =D $_{25}$ 0:32 and 0.43. The labels \$1' and \$2' refer to the two resolved spots in the center of NGC 4691,

whose colors were estimated from the images treated with the analog of CLEAN, with no error bars.

Fig. 7: b: NGC 337 and 4027, m agellanic barred spirals. The bar length was not estimated because it is dicult to delineate the bar precisely.

Fig. 8: Virgo galaxies which are not H $_{\rm I}$ -de cient. a: NGC 4178 and 4192.

Fig. 8:b:NGC 4351 and 4430.

Fig. 8:c: NGC 4567/8 and 4633.

Fig. 8:d:NGC 4634 and 4654.

Fig. 9: HI-de cient Virgo galaxies.a: NGC 4293 and 4388.

Fig. 9:b:NGC 4394 and 4413.

Fig. 9:c:NGC 4438 and 4450. The label Cp' refers to the nucleus of NGC 4435, which is likely at the origin of the disruption of NGC 4438 (Combes et al. 1988).

Fig. 9:d:NGC 4491 and 4498.

Fig. 9:e: NGC 4506 and 4569.

Fig. 9: f: NGC 4579 and 4580.

Fig. 9:g:NGC 4647 and 4689.

A cknow ledgem ents.

The DSS im ages shown here were retrieved from the ESO/ST-ECF Archive and were produced at the STScI. They are based on photographic data obtained using the Oschin Schm idt Telescope operated by Caltech and the Palom ar Observatory, and the UK Schm idt Telescope operated by the Edinburgh Royal Observatory.

The ISOCAM data presented in this paper were analyzed using and adapting the CIA package, a joint development by the ESA Astrophysics Division and the ISOCAM Consortium (led by the PIC.Cesarsky, Direction des Sciences de la Matiere, CEA, France).

R eferences

Athanassoula E., 1992, MNRAS 259, 345

Athanassoula E. & Martinet L., 1980, A & A 87, L10

BallR., Sargent A.I., Scoville N.Z., Lo K.Y. & Scott S.L., 1985, ApJ 298, L21

Bonnarel F., Boulesteix J., Georgelin Y.P. et al., 1988, A&A 189,59

BoselliA , Lequeux J., Sauvage M .et al., 1998, A & A 335, 53

Boselli A., Tu s R. J., Gavazzi G., Hippelein H. & Pierini D., 1997, A & A S. 121, 507

Bosm a A., van der Hulst JM . & Sullivan W .T., 1977, A&A 57,373

Buta R. & Crocker D A., 1993, AJ 105, 1344

Buta R., 1986, ApJS 61, 631

C esarsky C J., Abergel A., Agnese P. et al., 1996, A & A 315, L32

CombesF,DuprazC,CasoliF.& PaganiL,1988,A&A 203,L9

Coulais A. & Abergel A., 2000, A & AS 141, 533

Dale D A., Silberm ann N A., Helou G. et al., 2000, AJ 120,583

Desert F.-X., Boulanger F. & Puget J.L., 1990, A & A 237, 215

Dottori H A. & Pastoriza M G., 1986, RM xAA 12, 119
Feinstein C., Vega I., Mendez M. & Forte J.C., 1990, A & A
239, 90

Forbes D A., Norris R.P., Williger G.M. & Smith R.C., 1994, AJ 107, 984

Forster-Scheiber N M ., Laurent O ., Sauvage M . et al., 2001, subm itted to A & A

FriedliD., Wozniak H., Rieke M., Martinet L. & Bratschi P., 1996, A & A S 118, 461

Garc a-Barreto J.A., Franco J., Carrillo R., Venegas S. & Escalante-Ram rez B., 1996, RM xAA 32, 89

Garc a-Barreto JA, Franco J., Guichard J. & Carrillo R., 1995, ApJ 451, 156

Garca-Barreto JA., Downes D., Combes F., Carrasco L., Gerin M. & Cruz-Gonzalez I., 1991, A&A 252, 19

Guiderdoni B. & Rocca-Volmerange B., 1985, A&A 151, 108

Ham eed S.& Devereux N., 1999, AJ 118, 730

Hogbom JA., 1974, A&AS 15, 417

Jungwiert B., Combes F., Axon D.J., 1997, A&AS 125, 479

Kenney JD P.& Lord SD., 1991, ApJ 381, 118

M alhotra S., Helou G., van Buren D. et al., 1996, A & A 315, L161

Martin P. & Friedli D., 1997, A & A 326, 449

Martin P. & Belley J., 1997, A & A 321, 363

Martin P., 1995, AJ 109, 2428

M iville-D eschênes M A., Boulanger F., Abergel A. & Bernard J.P., 2000, in \ISO beyond point sources: studies of extended infrared em ission", ESA-SP 455, 27

M ollenho C., M atthias M. & Gerhard O. E., 1995, A & A 301, 359

Morgan W W ., 1958, PASP 70, 364

Odewahn S.C., 1994, AJ 107, 1320

Pence W D., Taylor K., Freem an K.C., de Vaucouleurs G. & Atherton P., 1988, ApJ 326, 564

Prendergast K.H., 1983, in Internal kinematics and dynamics of galaxies, IAU Symposium, 215

Regan M W , Teuben P J. & Vogel S N , 1996, A J 112, 2549

Regan M W . & Vogel S N ., 1995, ApJ 452, L21

Reynaud D. & Downes D., 1998, A&A 337, 671

Rice W., Lonsdale C.J., Soifer B.T. et al., 1988, ApJS 68,

Roussel H., Vigroux L., Sauvage M., Bosma A. et al., 2001a, submitted to A&A (Paper I)

Roussel H., Sauvage M. & Vigroux L., 2001b, submitted to A&A (Paper II)

Sandage A. & Bedke J., 1994, The Camegie at las of galaxies

Sandage A., 1961, The Hubble atlas of galaxies

SauvageM "B lom m aertJ., B oulangerF.etal., 1996, A & A 315, L89

Sersic J.L., 1973, PASP 85, 103

Sersic J.L. & Pastoriza M., 1965, PASP 77, 287

Starck J.L., AbergelA., AusselH. et al., 1999, A & AS 134, 135

Storchi-Bergm ann T., W ilson A.S. & Baldw in J.A., 1996, ApJ 460, 252

Tagger M . & Athanassoula E ., 1991, IAU Sym p. 146, 105 Tubbs A D ., 1982, ApJ 255, 458

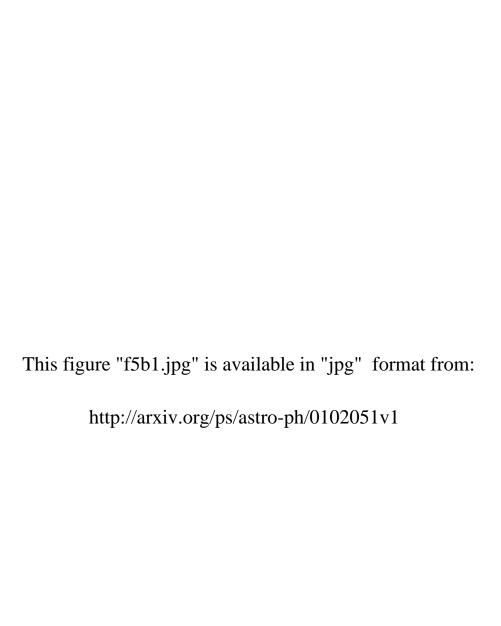
de Vaucouleurs G., de Vaucouleurs A., Corw in H.G. et al., 1991, Third Reference Cat. of Bright Galaxies (RC3)

Vogler A., Madden S., Sauvage M. et al., 2001, in preparation

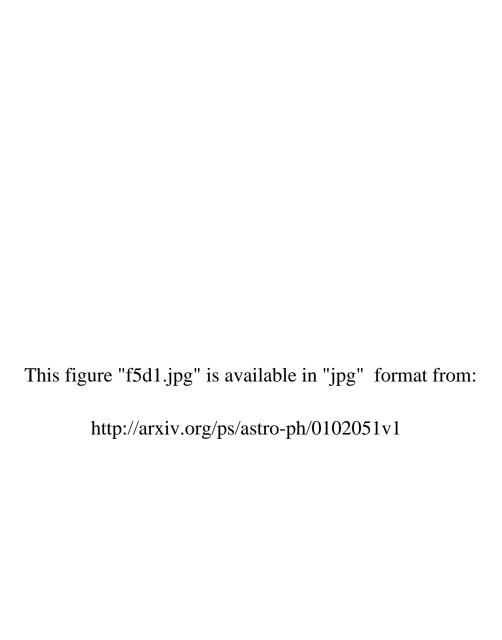
Wiklind T., Henkel C. & Sage L.J., 1993, A & A 271, 71 Zaritsky D. & Lo K.Y., 1986, ApJ 303, 66

This figure "f1.jpg" is available in "jpg" format from:

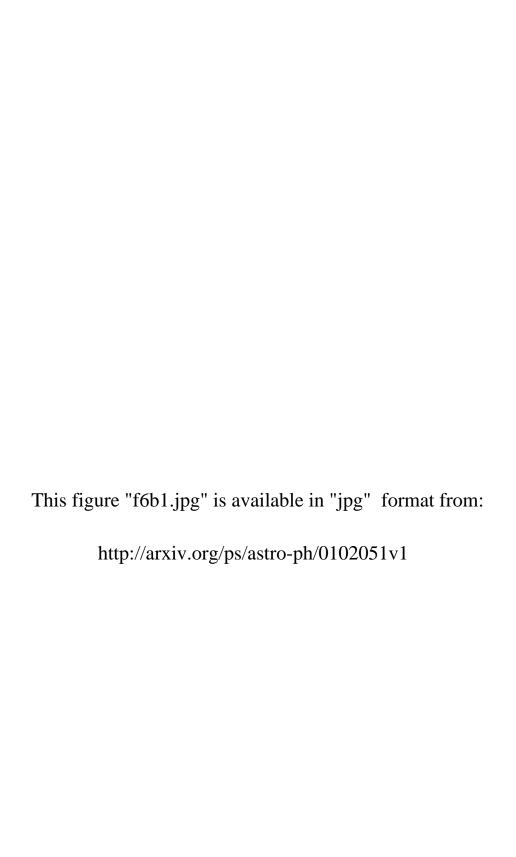
This figure "f5a1.jpg" is available in "jpg" format from:



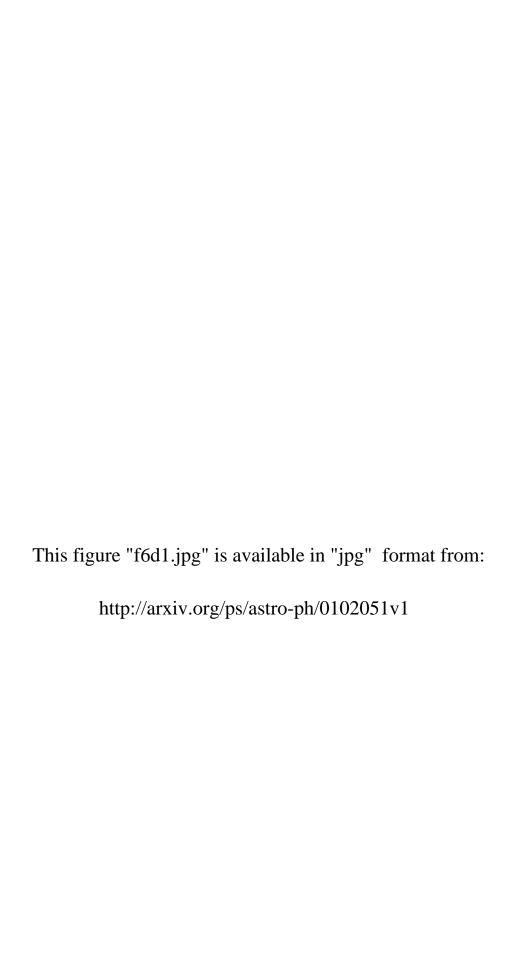
This figure "f5c1.jpg" is available in "jpg" format from:



This figure "f6a1.jpg" is available in "jpg" format from: http://arxiv.org/ps/astro-ph/0102051v1

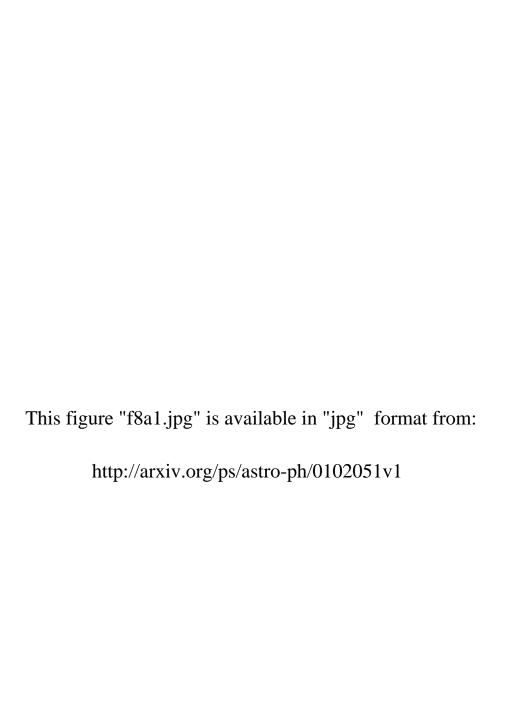


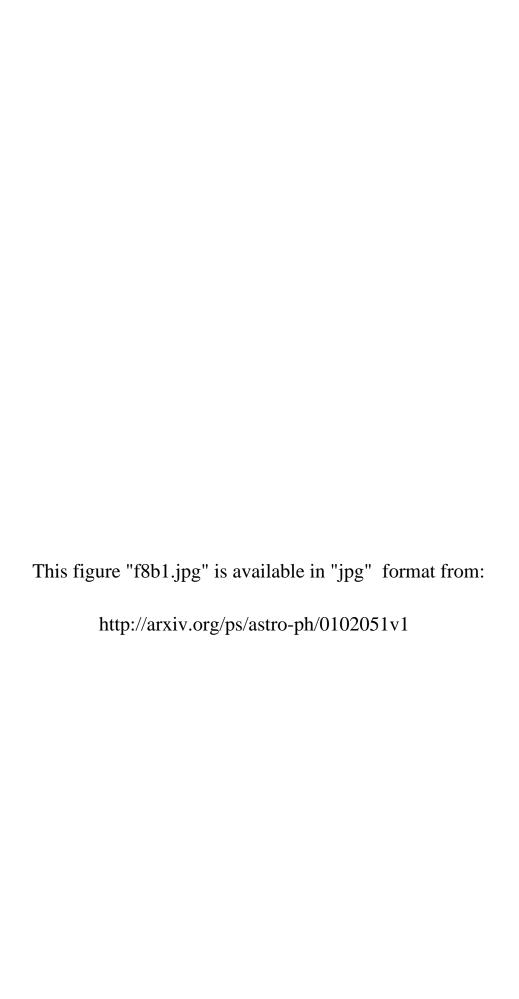
This figure "f6c1.jpg" is available in "jpg" format from:



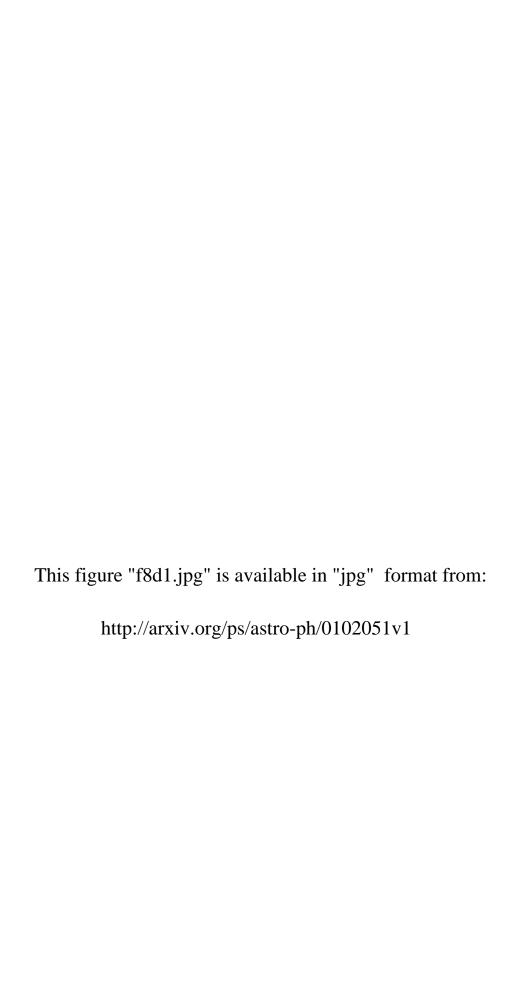
This figure "f7a1.jpg" is available in "jpg" format from:

This figure "f7b1.jpg" is available in "jpg" format from:

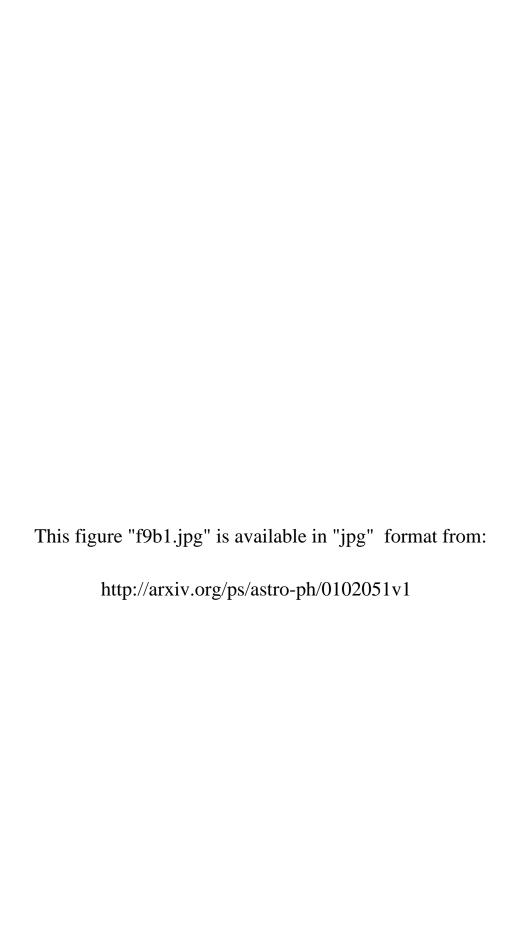




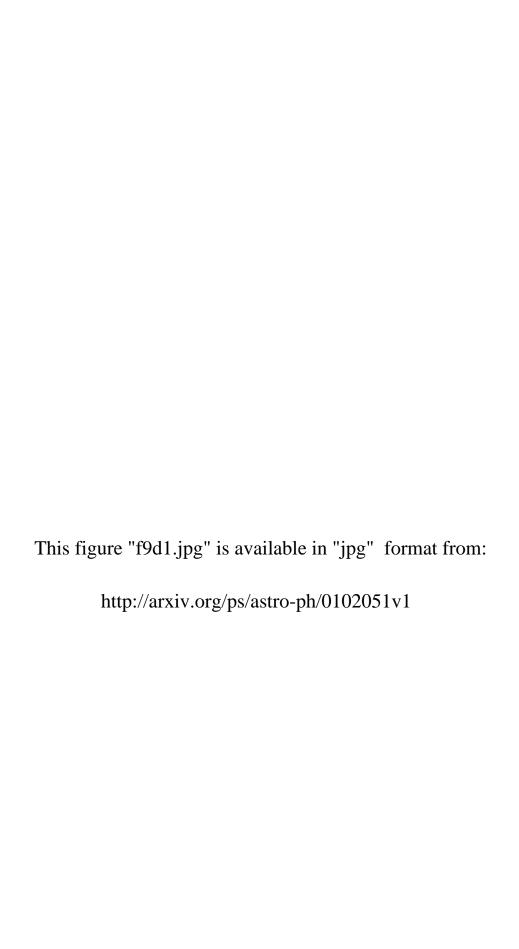
This figure "f8c1.jpg" is available in "jpg" format from:



This figure "f9a1.jpg" is available in "jpg" format from:



This figure "f9c1.jpg" is available in "jpg" format from:



This figure "f9e1.jpg" is available in "jpg" format from:

This figure "f9f1.jpg" is available in "jpg" format from:

This figure "f9g1.jpg" is available in "jpg" format from:

This figure "f2.jpg" is available in "jpg" format from:

This figure "f5a2.jpg" is available in "jpg" format from:

This figure "f5b2.jpg" is available in "jpg" format from:

This figure "f5c2.jpg" is available in "jpg" format from:

This figure "f5d2.jpg" is available in "jpg" format from:

This figure "f6a2.jpg" is available in "jpg" format from:

This figure "f6b2.jpg" is available in "jpg" format from:

This figure "f6c2.jpg" is available in "jpg" format from:

This figure "f6d2.jpg" is available in "jpg" format from:

This figure "f7a2.jpg" is available in "jpg" format from:

This figure "f7b2.jpg" is available in "jpg" format from:

This figure "f8a2.jpg" is available in "jpg" format from:

This figure "f8b2.jpg" is available in "jpg" format from:

http://arxiv.org/ps/astro-ph/0102051v1

This figure "f8c2.jpg" is available in "jpg" format from:

This figure "f8d2.jpg" is available in "jpg" format from: http://arxiv.org/ps/astro-ph/0102051v1

This figure "f9a2.jpg" is available in "jpg" format from:

This figure "f9b2.jpg" is available in "jpg" format from:

This figure "f9c2.jpg" is available in "jpg" format from:

This figure "f9d2.jpg" is available in "jpg" format from:

This figure "f9e2.jpg" is available in "jpg" format from:

This figure "f9f2.jpg" is available in "jpg" format from:

This figure "f9g2.jpg" is available in "jpg" format from:

This figure "f3a.jpg" is available in "jpg" format from:

This figure "f3b.jpg" is available in "jpg" format from:

This figure "f4a.jpg" is available in "jpg" format from:

This figure "f4b.jpg" is available in "jpg" format from: